Supplementary Information

Ballistic phonon transport in holey silicon by Jaeho Lee, Jongwoo Lim, Peidong Yang*

*E-mail: p_yang@berkeley.edu

Device Fabrication

Holey silicon devices are fabricated on commercial Silicon-on-Insulator (SOI) substrates (SOITEC) with a 200-nm-thick silicon device layer and a 150-nm-thick buried oxide layer. The silicon layer is p-type with a negligible doping concentration ($\sim 10^{15}$ cm^{-3}) and the crystal orientation is in the (100) direction. In order to vary the silicon layer thickness, the silicon was consumed by thermal oxidation and subsequently removed by wet etching. The thermal oxide layers were grown at 1000 °C for varying duration to provide 150 nm, 100 nm, 70 nm, and 35 nm thick silicon layers on the same SOI substrates. The varying thickness samples are then treated with identical processes in the following.

For patterning nano-holes over a large area, we utilized the self-assembly of block copolymer. 1% Poly(styrene-block-2-vinylpyridien) (PS-b-P2VP) block copolymer with molecular weight of 183.5kg mol^{-1} (M_n^{PS}=125 kg mol^{-1}; M_n^{P2VP}=58.5 kg mol^{-1}) was dissolved in toluene and stirred overnight. The polymer solution was spun cast on the SOI substrates. 300 ml toluene was used in a 200 ml jar as a solvent annealing method to induce lateral ordering of micro-domains. It was immersed in methanol for thirty minutes in order to reconstruct the P2VP part in the film and then blown by a nitrogen gun. The assembly of nano-holes with 60-nm-pitch patterns was confirmed by AFM and SEM.

To protect the polymer pattern during a silicon etching process, we used a chromium layer as a hard etch mask. The chromium was deposited by e-beam evaporator at 60 degrees. The controlled deposition thickness (5 – 9 nm) of the chromium determined the diameter of holes. The block copolymer layer under the chromium was removed by oxygen plasma generated at 50 W for 1 minute. Silicon trenches were then created by DRIE. The chromium was removed by immersing the samples in a chromium etchant solution (CR-7 from Cyantek) and also with oxygen plasma to ensure a clean surface. Even though we did not observe any defects using HRTEM and Raman spectroscopy, we post-annealed the samples at 800 °C in argon for two hours in order to remove any possible process-related surface defects.

Since the thermal conductivity measurement requires electrical isolation, we sputtered an 80-nm-thick silicon oxide layer over the holey silicon. The sputtered oxide also provides a smooth surface for subsequent processes. We confirmed with SEM that the sputtered oxide did not penetrate through the silicon trenches. Four-probe fabricated platinum electrodes were then fabricated using standard photolithography followed by metal deposition using an evaporator and lift-off in acetone. Using the platinum as a mask, we removed the oxide and the holey silicon outside the electrode using anisotropic dry etching processes. The sputtered oxide and holey silicon layers were first removed by CHF$_3$/Ar (80 sccm/4 sccm) under 80 mtorr at 150W, and the remaining holey silicon or thin film silicon layers were removed by DRIE. Potential CFx polymer residues were removed by oxygen plasma.

Sample Preparation for TEM and Raman spectroscopy

For Transmission Electron Microscopy (TEM) and Raman spectroscopy studies, the holey silicon layers were released from the SOI substrates and transferred to other substrates correspondingly. The buried oxide layer was first removed by vapor HF and then the silicon layers were detached from the substrates using a manipulator. For TEM measurements, the holey silicon layers were placed on a

copper grid and the images were taken by FEI Tecnai F-20 G2 S-TWIN. For Raman measurements, both holey silicon and thin-film silicon layers were transferred onto a silicon substrate covered with a tungsten layer. Confocal Raman spectroscopy (HORIBA LabRAM HR Evolution) was performed in backscattering configuration with a helium–neon laser (632.8nm wavelength) and a 100x 0.9NA objective. The laser power was set to 6.1 μW and the laser spot size was smaller than 1μm. The samples were heated to 50 °C using a hot stage for the measurements in ambient air.
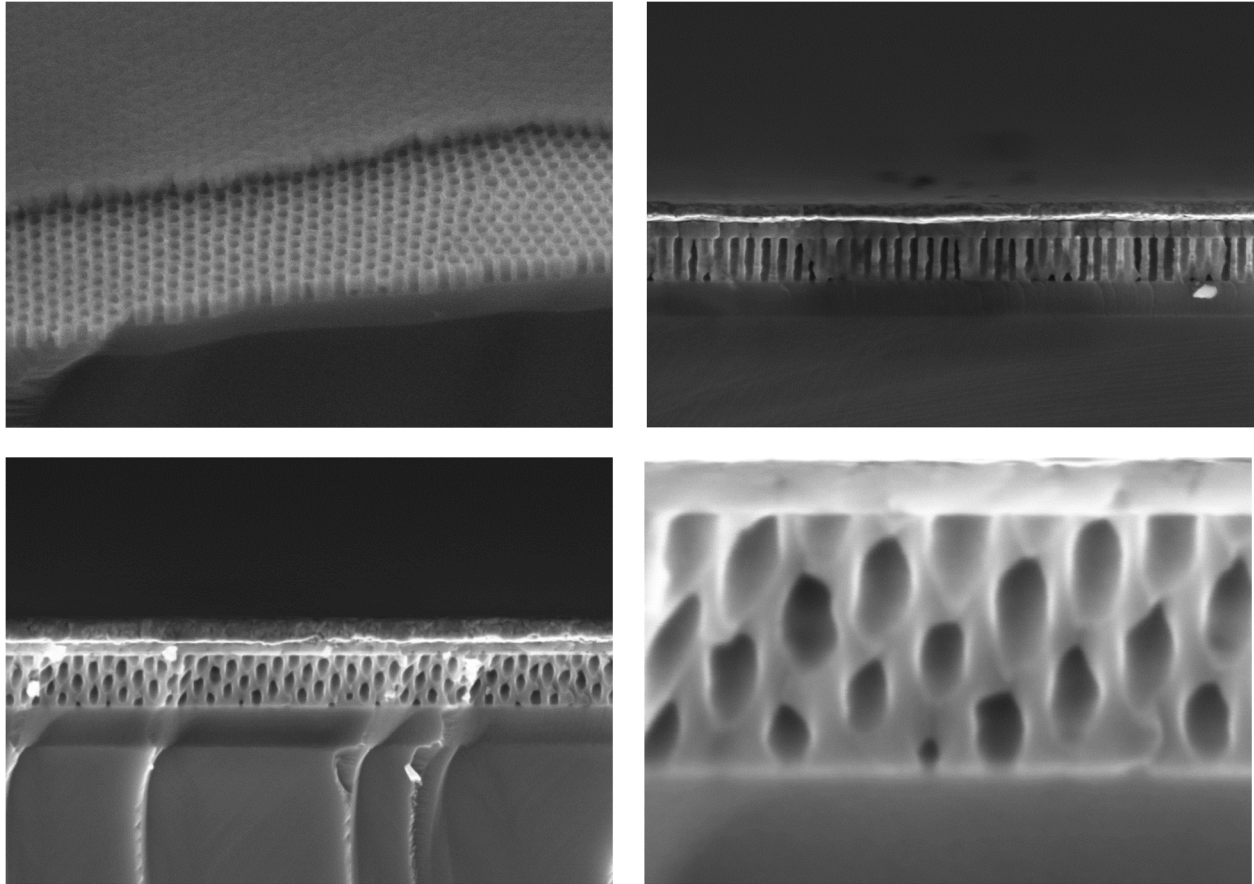

Figure S1. Side-view SEM images demonstrating smooth boundaries of holey silicon after DRIE. The contrast and non-uniform edges in cross-sectional images can be misleading due to cutting angles and defects created during the sample preparation. The SEM images do not show any scallops or rough boundaries in holey silicon, and we assume that holey silicon does not have any appreciable roughness that is relevant for long-wavelength phonons.

Raman Spectroscopy

Raman spectroscopy has been performed on both holey silicon and thin-film silicon samples to investigate potential impacts of dry etching and creating nano-holes on phonons, i.e. phonon localization, changes in anharmonicity, and strain effects[1-3]. For examples, phonon localization effect may red-shift and broaden Raman peaks by a relaxation of the fundamental phonon selection rule at the zone center[4]. Reactive ion etching processes may create nanocrystalline domains near the etched boundaries, which also lead to red-shifted and broadened Raman peaks[2,5]. However, our Raman data on holey silicon samples do not show a significant peak shift or broadening compared to that of thin-film

silicon samples. This indicates that our holey silicon may not have appreciable amounts of nanocrystalline domains or defects, which is also consistent with HRTEM images. Since Raman peaks are sensitive to temperature, the temperature of the sample is carefully controlled by a heater stage and the excitation laser power is kept low to minimize local heating. The local heating effect is subject to the thermal conductance and the thermal contact resistance of each sample, and this can lead to a variation in Raman spectrum. The peak position and the full-width at half-maximum (FWHM) values of thin-film silicon samples are 520.45 ± 0.02 cm^{-1} and 3.27 ± 0.01 cm^{-1}, respectively. The peak position and the FWHM values of holey silicon samples are 520.18 ± 0.10 cm^{-1} and 3.53±0.18 cm^{-1}, resepctively. The stage temperature was at 50°C. The difference between the two samples is within the measurement uncertainty, and we assume the Raman red-shfitng or broadening effects is not significant in our samples. However, more precise understanding of the Raman spectra requires further investigation, e.g. temperature dependent studies.
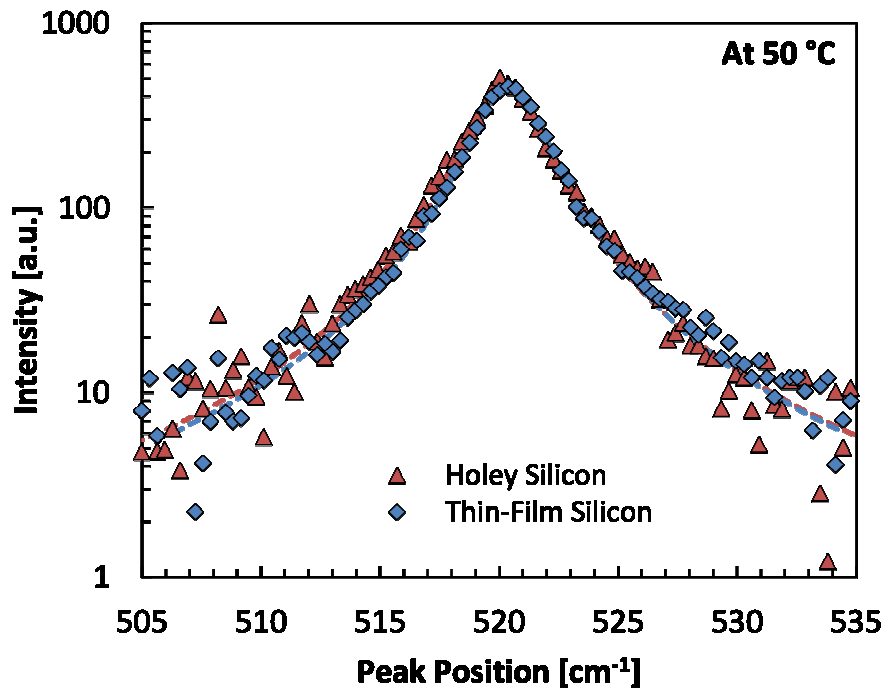

Figure S2. Raman spectroscopy data at 50 °C. The full-width at half-maximum (FWHM) is 3.33 cm^{-1} for holey silicon and 3.27 cm^{-1} for thin-film silicon, and their difference is within the measurement uncertainty.

Experimental Method

The 3ω measurements[20, 21] on holey silicon devices can be sensitive to variations in thermal conductivity, boundary resistance, and heat capacity of surrounding materials such as sputtered oxide, buried oxide, and silicon substrate. In order to extract the thermal conductivity of holey silicon, we reduce the number of unknown variables and maximize the measurement sensitivity to holey silicon by following. Firstly, we modulate the thermal diffusion depth by controlling the heating frequency[21]. When the thermal diffusion depth is much larger than the layer thicknesses, the measurement becomes insensitive to their heat capacity. At the same time, the thermal diffusion depth should be shorter than

the substrate thickness in order to remove the unknown boundary resistance at the bottom of the substrate. By keeping the heating frequency to 100 Hz – 2 kHz, we maximize the measurement sensitivity to the thermal conductivities of holey silicon and oxide layers. With the modulated diffusion depth, the 3ω measurement is also insensitive to convection or radiation heat losses[20].

Secondly, we force heat conduction in the cross-plane direction by fabricating a vertical stack in measurement devices. Using DRIE, we removed the silicon and oxide layers that are outside platinum heaters. The heat conduction across holey silicon and oxide layers become one-dimensional, and the measurements become insensitive to unknown anisotropy ratios or in-plane thermal conductivities. The one-dimensional design also allows the use of narrow heaters that are otherwise susceptible to lateral heat spreading. The heat conduction solution is more sensitive to the holey silicon layer when the heater is narrow because the narrow heaters confine more heating to the vertical stack including the holey silicon layer.

Thirdly, we obtain the thermal properties of oxide layers and substrates from control devices. We assume holey silicon and control devices share the same thermal conductivity and boundary resistances for the oxide layers and the substrate. This is based on the assumption that holey silicon and control devices share the same thermal properties in the SiO_2 layers and the Si substrate, and the only difference is the cross-sectional areas of holey silicon and thin film control devices, which are treated with the measured porosity from the image processing characterization. We also assume any geometric effects such as phonon crowding are negligible in the sputtered SiO_2 because the phonon mean free path is very small in the amorphous material. We use a theoretical value for silicon films. However, the thermal conductivity of silicon films is expected to be much higher than that of oxides and their contribution is less than 2% to the total thermal resistance. Therefore, a deviation from the theoretical value has little impact on the measurement. The BTE modeling assuming diffusive boundaries predicts that the lower-bound thermal conductivity of silicon films for 200 nm, 100 nm, and 35 nm thickness is 63 $Wm^{-1}K^{-1}$, 48 $Wm^{-1}K^{-1}$, and 30 $Wm^{-1}K^{-1}$ respectively. Their upper bound thermal conductivity assuming specular boundaries reaches the bulk silicon value, which is 150 $Wm^{-1}K^{-1}$. Since the effective thermal conductivity of holey silicon ranges from 1 $Wm^{-1}K^{-1}$ to 6 $Wm^{-1}K^{-1}$, the differential analysis is much more sensitive to the holey silicon thermal conductivity. The sensitivity to holey silicon also increases further when the porosity is higher because the effective thermal resistance of holey silicon becomes much greater than that of thin-film silicon. For porosity 30% or higher, the measurement uncertainty to the holey silicon thermal conductivity in the differential analysis is 6 % or lower.

Low Temperature Experiment

We used a commercial cryostat (CTI model 22 refrigerator) to control the measurement temperature down to 16 °K. The actual sample temperature was measured using a custom thermocouple that was positioned in the identical position with the sample. The measurement temperature below 30 °K was broken into steps of 2 °K, and only the data down to 20 °K was reported because the temperature coefficient of resistance (TCR) measurement requires at least three data points at different temperatures. At each temperature, the feedback system was given sufficient time (> 20 min) to stabilize and the temperature stabilization was monitored until a change in temperature was less than 0.03 °K in five minutes.

Classical Modeling Based on Boltzmann Transport Equation

In general, the Boltzmann Transport Equation (BTE) is a great resource to understand phonon transport in semiconductors. Researchers have successfully matched BTE solutions to the thermal

conductivity data for bulk silicon[6,7], silicon thin films[8,9], silicon nanowires[10,11] and nanoporous silicon[12-14]. Modeling silicon nanostructures are based on bulk silicon dispersion, which is known to provide an accurate description of phonon states in silicon as thin as 5 nm[15,16]. This work uses quadratic fits tracking acoustic and optical phonon dispersion branches from a neutron scattering experiment[17,18]. We consider the phonon dispersion in silicon along the (100) direction and assume each phonon dispersion branch is isotropic. We use a BTE solution under the relaxation time approximation and use the Matthiessen's Rule to capture various scattering events. The cross-plane thermal conductivity can be expressed as,

$$K = \frac{1}{8\pi^2} \sum_n \int_0^{k_o} \int_0^{2\pi} \int_0^{\pi} C_{ph} \, v_g^2 \, \tau \, k^2 sin\theta \, d\theta d\phi dk$$

where the heat capacity (C_{ph}), group velocity (v_g), total relaxation time (τ), are each dependent on the phonon frequency (ω) and the wave vector (k). The total relaxation time ($\tau^{-1} = \tau_U^{-1} + \tau_D^{-1} + \tau_{bl}^{-1} + \tau_{bv}^{-1}$) accounts for the Umklapp scattering (τ_U), point-defect scattering (τ_D), lateral boundary scattering (τ_{bl}) and vertical boundary scattering (τ_{bv}). The relaxation time due to the Umkapp scattering can be expressed as $\tau_U = AT\omega^2 exp(-B/T)$ where A = 1.4×10^{-19} s/K and C = 152 K are the fitting parameters that reproduce the bulk silicon thermal conductivity[13]. The relaxation time due to phonon-defect scattering can be expressed as $\tau_D = D\omega^4$. For nearly pure silicon, the parameter D mainly depends on the isotope concentration and has been determined as D = 1.32 x 10^{-45} s^3[15]. The model has successfully matched the bulk silicon data and other modeling work in literature[6-14].

The boundary scattering terms define the size effect in nanostructures. The vertical boundary scattering at top and bottom interfaces of holey silicon bounded in the length (L) is $\tau_{bl} = L/(2 \, v_{ph} cos\theta)$. For modeling the lateral boundary scattering, we assume the cross-sectional area of a holey silicon unit cell is equivalent to that of a nanowire. In the worst-case scenario, phonons scatter diffusely at the boundaries defined by the neck size, as if they are passing through a nanowire of the diameter equivalent to the neck size (n = 20 nm), and we use $\tau_{bl} = (4/3\pi) \, n/(v_{ph} sin\theta)$. The nanowire analogy provides the lower bound thermal conductivity, and the thin-film silicon analogy provides the upper bound thermal conductivity (Fig. S3). Our BTE predictions are consistent with Dresselhaus modeling results[12], which use a more sophisticated modeling for periodic nanoporous silicon, and other literature studies. However, the classical predictions do not match the experimental data of length-dependent holey silicon samples.
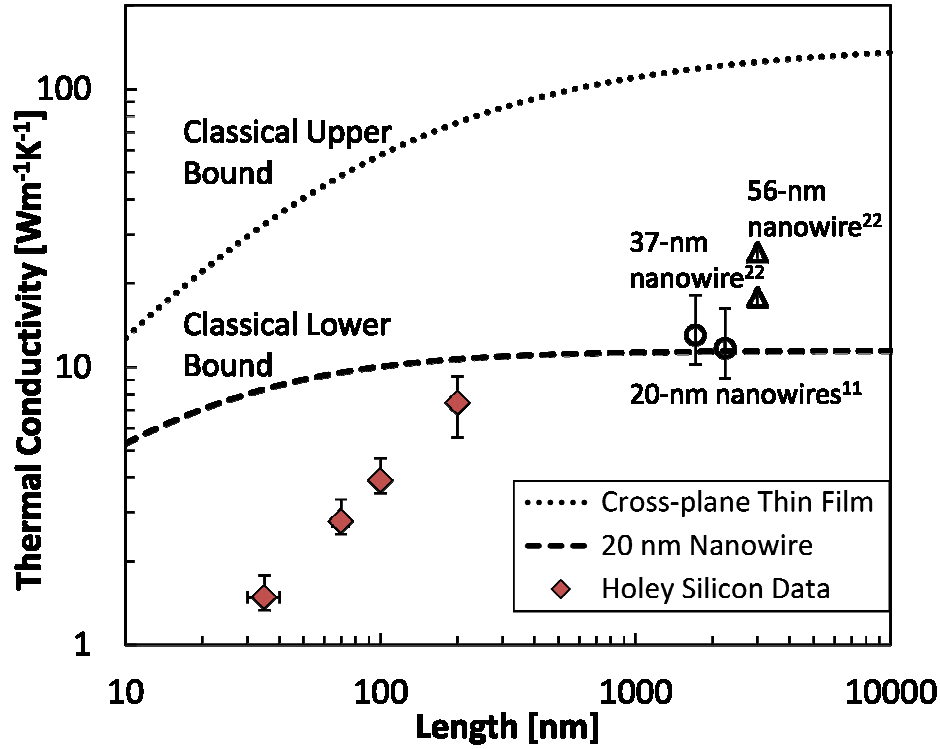
Figure S3. Room-temperature thermal conductivity of 20-nm-neck holey silicon of varying length. The upper bound of holey silicon thermal conductivity we can predict using the classical BTE model is equivalent to the cross-plane thermal conductivity of silicon thin films. This is based on the assumption that the lateral boundaries in holey silicon are completely specular. The classical lower bound is the thermal conductivity of 20-nm-wide nanowires, and this is based on the assumption that the lateral boundaries in holey silicon are completely diffuse and the channel is limited to the neck size. The thermal conductivity of holey silicon exhibits greater size effect than the classical predictions, indicating the presence of unique phonon transport phenomena.

Semi-Empirical Modeling Based on Landauer Formulism

While classical BTE models struggled to match the thermal conductivity data of thin nanowires, a Landauer formulism developed by Murphy *et al.*[19] and Chen *et al.*[11] has successfully captured the thermal conductivity data of silicon nanowires. The thermal conductance (*G*) of a quasi-one-dimensional nanostructure can be expressed as

$$G = \frac{k_B}{2\pi} \int_0^\infty \left(\frac{N_1}{1+L/l} + \frac{N_2}{1+L/d} \right) \frac{X^2 \exp(X)}{(\exp(X)-1)^2} \, d\omega$$

where *d* is the diameter, *l* is the frequency dependent mean free path, N_1 is the number of modes with the mean free path *l*, and N_2 is the number of modes with the mean free path limited to *d*, and $X = \hbar\omega/k_B T$. The total number of modes at a given frequency is given by $N = 4 + A(d/a)^2 (\omega/\omega_d)^2$ where *a* is the lattice spacing, the factor 4 corresponds to the four modes (longitudinal, torsional, and two flexural), *A* is a fitting parameter and ω_d is the Debye cut-off frequency. N_1 is given by $N(\min(\omega, c/h))$ where *h* is

the length scale of surface disorder and c is the sound velocity, and N_2 is defined by $N - N_1$. The frequency dependent mean free path due to lateral boundary scattering can be expressed as,

$$l_o = \left(4B \frac{h^2}{d^3} \left(\frac{\omega}{\omega_D} \right)^2 + AB \frac{h^2}{a^2 d} \left(\frac{\omega}{\omega_D} \right)^4 \right)^{-1}$$

where A and B are the dimensionless constants used as fitting parameters. When the wavelength is longer than the length scale of surface disorder, the mean free path becomes l and when the wavelength is shorter the mean free path becomes d. In other words, this model combines incoherent surface scattering for short-wavelength phonons with nearly ballistic long-wavelength phonons.

This model captures the thermal conductivity of nanowires and the non-classical temperature dependence at T < 100 °K by accounting for an increased contribution of specular scattering by low frequency phonons.

The past work[11,19] does not include Umklapp scattering and point-defect scattering, but we include them by using $l_t^{-1} = l_o^{-1} + l_U^{-1} + l_D^{-1}$ where l_U and l_D are the same expressions from the BTE model. We have also included a correction in the cut-off frequency due to Umklapp scattering as suggested by Mingo[15]. Figure 4 in the manuscript shows the mean free path of low frequency phonons is limited by Umklapp scattering that scales by ω^{-2} and the mean free path of high frequency phonons is limited by lateral boundary scattering that scales by ω^{-4}. The frequency dependence here resembles scattering from point-like impurities. It treats disorder as a collection of point-like impurities.

We fit the length dependent thermal conductivity by introducing a vertical boundary scattering effect using the scaling model (eq. 3 in the main article) assuming the scattering at top and bottom interfaces are completely diffuse. We find the fitting parameters A = 1.4 and B = 0.2 best match the holey silicon data. The length scale of surface disorder is assumed as h = 1.5 nm based on the observation made in the TEM analysis. The assumptions made in favor to fit the length dependent thermal conductivity data result in a significant contribution of specular scattering by low frequency phonons (Fig. S4). The specular scattering at lateral boundaries might be responsible for the length dependent thermal conductivity in the holey silicon.

The scaling models predict that the thermal conductivity of infinitely-long holey silicon reaches the reported thermal conductivity of nanowires with the equivalent cross-sectional area. The equivalent cross-sectional areas can be estimated based on limiting dimensions in a hexagonal lattice (Fig. S5).
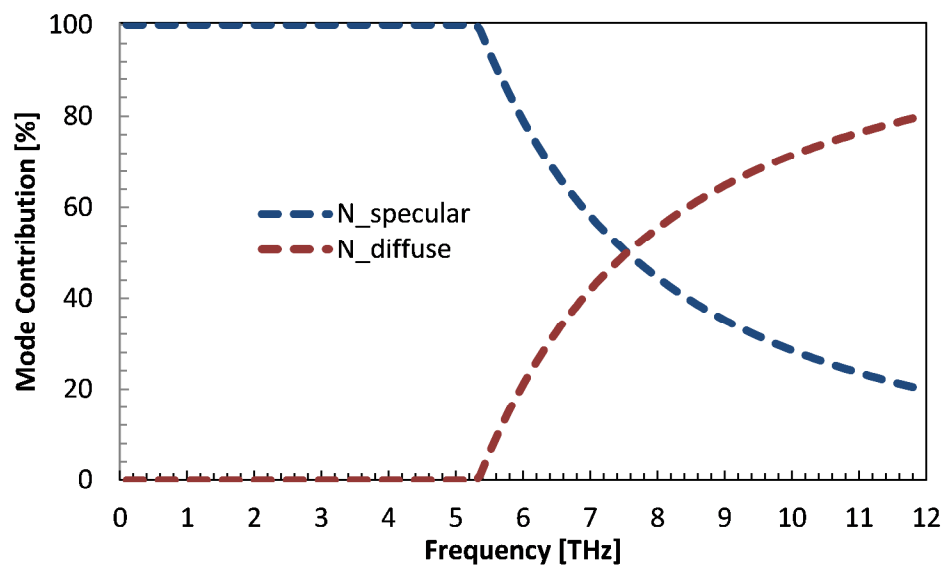
Figure S4. Frequency dependent contributions of specular and diffuse scattering at lateral boundaries. The specular scattering is favored at low frequencies while the diffuse scattering is favored at high frequencies. This is because the low frequency phonons have relatively longer wavelength and are less susceptible to surface disorder.
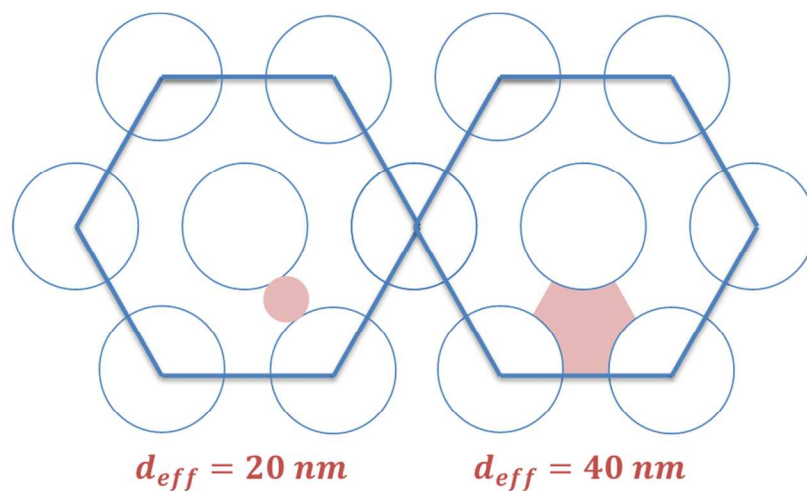

$$d_{eff} = 20 \ nm \qquad d_{eff} = 40 \ nm$$

Figure S5. Effective diameter (d_{eff}) estimation for the cross-sectional area of a holey silicon unit cell. The scaling models show the thermal conductivity of infinitely-long holey silicon reaches the reported thermal conductivity of nanowires with the equivalent cross-sectional area.

Length Dependent Thermal Conductivity at Different Temperatures

Ballistic phonon transport is expected to be stronger at lower temperatures because phonon population is smaller and the Umklapp scattering is weaker. Figure S6 shows the length dependent thermal conductivity of 20-nm-neck holey silicon at 50, 100, and 300 K. The 300 K data is equivalent to the Figure 3 of the main article, but the data sets are obtained from low temperature experiment. The length dependences at 100 K and 50 K also show that ballistic transport is dominant. This trend validates strong presence of ballistic phonons in holey silicon structures as explained by the mean free path arguments.
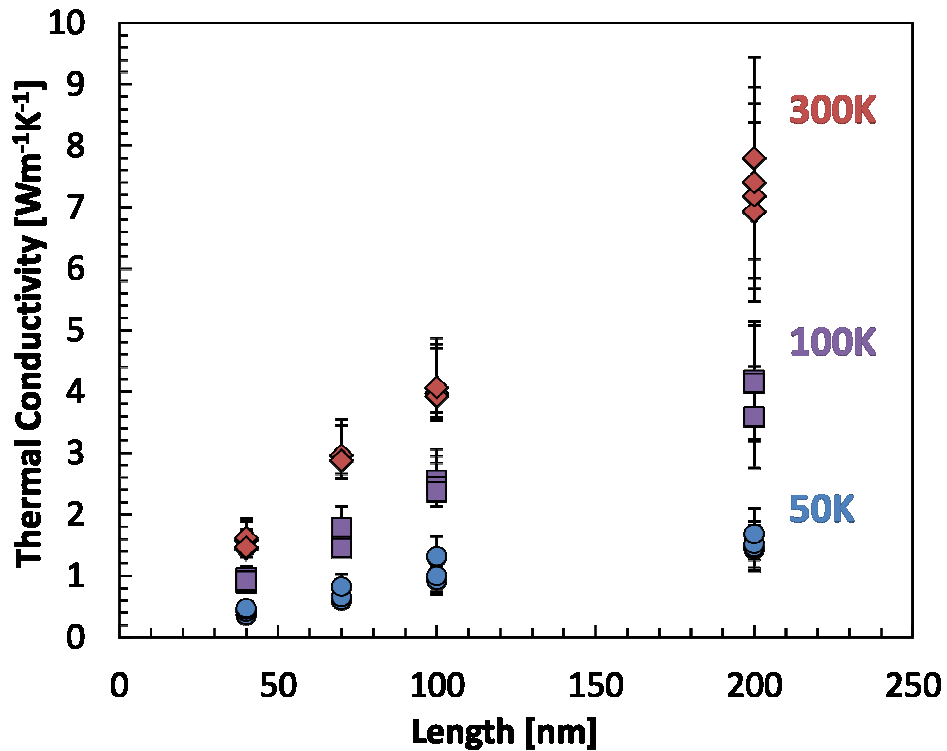

Figure S6. Length dependent thermal conductivity of holey silicon at different temperatures. The data in this figure is selected from the low temperature data in Figure 5 of the main article. The length dependence indicates ballistic transport is dominant through all temperature range explored in this work.

Reference

1. N. Fukata, T. Oshima, K. Murakami, T. Kizuka, T.Tsurui and S. Ito, Phonon confinement effect of silicon nanowires synthesized by laser ablation, Appl. Phys. Lett. 86, 213112-213115 (2005)
2. S.G. Cloutier, C.H. Hsu, P.A. Kossyrev, and J. Xu, Enhancement of Radiative Recombination in Silicon via Phonon Localization and Selection-Rule Breaking, Adv. Mater. 18, 841-844,(2006)
3. G.S. Doerk, C.Carraro, and R.Maboudian, "Temperature dependence of Raman spectra for individual silicon nanowires", Phys. Rev. B. 80, 073306-073310 (2009)

4. Z. Sui, P.P. Leong, I.P.Herman, "Raman analysis of light-emiiting porous silicon", Appl. Phys. Lett. 50, 2086-2088, (1992)

5. K. W. Adu, H. R. Gutie´rrez, U. J. Kim, G. U. Sumanasekera, and P. C. Eklund "Confined Phonons in Si Nanowires" Nano Letters, 5, 409–414, (2005)

6. J. Callaway, Model for Lattice Thermal Conductivity at Low Temperatures, Physical Review, Vol. 113, pp. 1046–1051, 1959.

7. M.G. Holland, Analysis of Lattice Thermal Conductivity, Physical Review, Vol. 132, p. 2461-2471, 1963.

8. W. Liu and M. Asheghi, Thermal Conductivity Measurements of Ultra-Thin Single Crystal Silicon Layers, Journal of Heat Transfer, Vol. 128, pp. 75–83, 2006.

9. Ju, Y. S. & Goodson, K. E. Phonon scattering in silicon films with thickness of order 100 nm. Appl. Phys. Lett. 74, 3005-3007 (1999).

10. M. G. Ghossoub, K. V. Valavala, M. Seong, B. Azeredo, K. Hsu, J. S. Sadhu, P. K. Singh, and S. Sinha, "Spectral Phonon Scattering from Sub-10 nm Surface Roughness Wavelengths in Metal-Assisted Chemically Etched Si Nanowires," *Nano Lett*. 13(4), 1564–1571 (2013).

11. Chen, R.; Hochbaum, A. I.; Murphy, P.; Moore, J.; Yang, P.; Majumdar, A., "Thermal Conductance of Thin Silicon Nanowires," *Phys. Rev. Lett*. 2008, 101, 105501-105505

12. Yang, R., Chen, G. & Dresselhaus, M.S. Thermal conductivity of simple and tubular nanowire composites in the longitudinal direction. *Physical Review B* 72, 125418-125425 (2005).

13. P.E. Hopkins, C.M. Reinke, M.F. Su, R.H. Olsson, E.A. Shaner, Z.C. Leseman, J.R. Serrano, L.M. Phinney, and I. El-Kady, Reduction in the Thermal Conductivity of Single Crystalline Silicon by Phononic Crystal Patterning, *Nano Letters*, Vol. 11, pp. 107–112, 2010.

14. Marconnet, A. M., Kodama, T., Asheghi, M., and Goodson, K. E., 2012, "Phonon Thermal Conduction in Periodically Porous Silicon Nanobridges," *Microscale Nanoscale Therm. Eng*., 16(4), pp. 199–219

15. Mingo, N. Calculation of Si nanowire thermal conductivity using complete phonon dispersion relations. *Phys. Rev. B* (2003), 68 (11), 113308-113312.

16. Prasher, R., Tong, T. & Majumdar, A. Approximate analytical models for phonon specific heat and ballistic thermal conductance of nanowires. *Nano Lett*. 8, 99-103, (2008).

17. G. Dolling, Lattice vibration in crystals with diamond structures, in: I. Vienna (Ed.), Symposium on Inelastic Scattering Neutrons in Solids and Liquids, vol. 2, Chalk River, 1963, pp. 37-48.

18. E. Pop, R. Dutton, K. Goodson, Analytic band Monte Carlo model for electron transport in Si including acoustic and optical phonon dispersion, J. Appl. Phys. 96 (2004) 4998-5005.

19. Murphy, P. G.; Moore, J. E. Coherent phonon scattering effects on thermal transport in thin semiconductor nanowires. Phys. Rev. B (2007), 76 (15), 155313-155324.

20. Cahill, D. G. Thermal conductivity measurement from 30 to 750 K: the 3ω method. Rev. Sci. Instrum. 61 (2), pp. 802–808, (1990).

21. Lee, J., Li, Z., Reifenberg, J. P., Lee, S., Sinclair, R., Asheghi, M. & Goodson, K. E. Thermal conductivity anisotropy and grain structure in Ge2Sb2Te5 films. J. Appl. Phys. 109, 084902-084908 (2011).

22. Li, D.; Wu, Y.; Kim, P.; Shi, L.; Yang, P.; Majumdar, A. "Thermal conductivity of individual silicon nanowires," Appl. Phys. Lett. 83, 2934–2936 (2003).